The Bonding Electron Density in Aluminum

Philip N. H. Nakashima, *et al.*

Science **331**, 1583 (2011);
DOI: 10.1126/science.1198543

14. J. E. Hoffman *et al.*, *Science* **295**, 466 (2002).
15. C. Howald, H. Eisaki, N. Kaneko, A. Kapitulnik, *Proc. Natl. Acad. Sci. U.S.A.* **100**, 9705 (2003).
16. M. Vershinin *et al.*, *Science* **303**, 1995 (2004).
17. Y. Kohsaka *et al.*, *Science* **315**, 1380 (2007).
18. C. V. Parker *et al.*, *Nature* **468**, 677 (2010).
19. W. D. Wise *et al.*, *Nat. Phys.* **4**, 696 (2008).
20. V. Hinkov *et al.*, *Science* **319**, 597 (2008).
21. R. Daou *et al.*, *Nature* **463**, 519 (2010).
22. M. J. Lawler *et al.*, *Nature* **466**, 347 (2010).
23. A. Kaminski *et al.*, *Nature* **416**, 610 (2002).
24. B. Fauqué *et al.*, *Phys. Rev. Lett.* **96**, 197001 (2006).
25. J. Xia *et al.*, *Phys. Rev. Lett.* **100**, 127002 (2008).
26. Y. Li *et al.*, *Nature* **455**, 372 (2008).
27. Materials and methods are available as supporting material on *Science* Online.
28. J. Xia, Y. Maeno, P. T. Beyersdorf, M. M. Fejer, A. Kapitulnik, *Phys. Rev. Lett.* **97**, 167002 (2006).
29. M. Hashimoto *et al.*, *Nat. Phys.* **6**, 414 (2010).
30. G. L. Eesley *et al.*, *Phys. Rev. Lett.* **65**, 3445 (1990).
31. P. Gay *et al.*, *J. Low Temp. Phys.* **117**, 1025 (1999).
32. J. Demsar *et al.*, *Phys. Rev. Lett.* **82**, 4918 (1999).
33. R. A. Kaindl *et al.*, *Science* **287**, 470 (2000).
34. N. Gedik *et al.*, *Phys. Rev. B* **70**, 014504 (2004).
35. E. E. M. Chia *et al.*, *Phys. Rev. Lett.* **99**, 147008 (2007).
36. Y. H. Liu *et al.*, *Phys. Rev. Lett.* **101**, 137003 (2008).
37. A. V. Fedorov *et al.*, *Phys. Rev. Lett.* **82**, 2179 (1999).
38. That this is a bulk superconducting effect is corroborated by the magnetic field-dependent suppression of the Knight shift (a measure of the density of states at E_F) seen below T_c of Bi2201 in nuclear magnetic resonance (*40*). The Knight shift was found to drop sharply at T^*, exhibiting a similar temperature dependence as those shown in Fig. 3.
39. S. V. Borisenko *et al.*, *Phys. Rev. Lett.* **102**, 166402 (2009).
40. S. Kawasaki, C. Lin, P. L. Kuhns, A. P. Reyes, G. Q. Zheng, *Phys. Rev. Lett.* **105**, 137002 (2010).

41. We thank I. Vishik, W.-S. Lee, L. Taillefer, and M. Greven for helpful discussions, Y. Li and G. Yu for experimental assistance on SQUID, and J.-H. Chu on resistivity measurements. R.-H.H. thanks the SGF for financial support. This work at the Stanford Institute for Materials and Energy Sciences, the Stanford Synchrotron Radiation Lightsource, and the Advanced Light Source is supported by the Department of Energy, Office of Basic Energy Sciences under contracts DE-AC02-76SF00515 and DE-AC02-05CH11231.

Supporting Online Material

www.sciencemag.org/cgi/content/full/331/6024/1579/DC1
Materials and Methods
SOM Text
Figs. S1 to S8
References

28 September 2010; accepted 15 February 2011
10.1126/science.1198415

The Bonding Electron Density in Aluminum

Philip N. H. Nakashima,[1,2,3]* Andrew E. Smith,[1,4] Joanne Etheridge,[2,3] Barrington C. Muddle[1,2]

Aluminum is considered to approach an "ideal" metal or free electron gas. The valence electrons move freely, as if unaffected by the presence of the metal ions. Therefore, the electron redistribution due to chemical bonding is subtle and has proven extremely difficult to determine. Experimental measurements and ab initio calculations have yielded substantially different results. We applied quantitative convergent-beam electron diffraction to aluminum to provide an experimental determination of the bonding electron distribution. Calculation of the electron distribution based on density functional theory is shown to be in close agreement. Our results yield an accurate quantitative correlation between the anisotropic elastic properties of aluminum and the bonding electron and electrostatic potential distributions.

The electronic structure associated with chemical bonding affects all properties of materials except radioactivity. In metals, the widely taught concept of an ideal metal or free electron gas is popularly expressed as a regular array of metal ions surrounded by a sea of delocalized valence electrons (*1*). Although a gross simplification, this model is often sufficient to give a qualitative account of many characteristic properties of metals such as their high electrical and thermal conductivities and lustrous or shiny appearance (*1*–*3*). However, it fails to explain the often strong variation in particular properties of different metals that are sensitive to electronic structure (*2*–*4*)—for example, the anisotropy of elastic constants. One of the best examples of a free electron gas is aluminum (*2*, *5*).

Aluminum accounts for more than 40% of world production in nonferrous metals (*6*). The large global effort invested in refining aluminum and its alloys to extend property profiles involves the need for a fundamental understanding of metallic structure in solid solutions and structural evolution at the nanoscale in multiphase alloys. Such an effort must begin with accurate knowledge of the electronic structure, chemical bonding, and atomic-scale mechanics in pure aluminum (*2*–*4*, *7*–*12*), and then ultimately extend to its alloys (*2*, *8*, *9*, *13*).

A difficulty arising from aluminum's close approximation to a free electron gas is that the perturbation of the total electron distribution by chemical bonds is subtle and difficult to determine. As a consequence, extensive experimental and theoretical studies of the electron density in aluminum have been carried out since the 1920s (*7*, *8*, *14*–*17*) but have failed to reach a consensus on the electronic structure of the chemical bonds. All possible modes are represented in the literature, including bridge bonding between nearest neighbors (*17*), octahedrally centered bonding between second nearest neighbors (*7*, *17*), tetrahedrally centered bonding between nearest neighbors (*8*, *17*), and mixtures of these modes (*17*).

Using quantitative convergent-beam electron diffraction (QCBED), we have made absolute measurements of electronic structure at ambient and liquid helium–cooled temperatures that are of sufficient accuracy, precision, and resolution to establish the bonding electron distribution in aluminum unequivocally. Electron diffraction is intrinsically sensitive to electron distribution by virtue of the strong interaction of the electron with the electrostatic potential of the specimen. Using Wien2K (*18*), we performed an ab initio density functional theory (DFT) calculation of the electron distribution [using the generalized gradient approximation (GGA) in the full potential linearly augmented plane wave formalism (FPLAPW), incorporating local orbital and local screening potentials (lo + ls)] and found that it agrees closely with the experimental determination by QCBED. The bonding electron and potential distributions determined here have a strong quantitative correlation with the anisotropy of Young's modulus for aluminum.

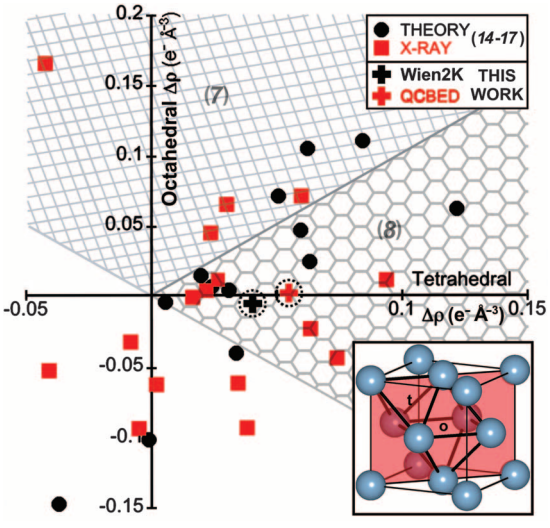

Fig. 1. Sets of F_g published since 1929 (*14*–*17*) are plotted as points on the graph of $\Delta\rho_{oct}$ at the octahedral site versus $\Delta\rho_{tet}$ at the tetrahedral site (o and t, respectively, in the inset). The DFT calculations of (*7*) would lie in the cross-hatched region of $\Delta\rho_{oct} > \Delta\rho_{tet}$. The full potential linear muffin tin orbital (FPLMTO) calculations of (*8*) would lie in the hexagon-hatched region of $\Delta\rho_{tet} > \Delta\rho_{oct}$. The present QCBED and Wien2K DFT (GGA/FPLAPW +lo +ls) (*18*) results are shown as circled crosses. See fig. S1 (*17*) for references for all points. All $\Delta\rho$ values were computed using the Eden Crystallography package (*29*).

[1]ARC Centre of Excellence for Design in Light Metals, Monash University, Victoria 3800, Australia. [2]Department of Materials Engineering, Monash University, Victoria 3800, Australia. [3]Monash Centre for Electron Microscopy, Monash University, Victoria 3800, Australia. [4]School of Physics, Monash University, Victoria 3800, Australia.

*To whom correspondence should be addressed. E-mail: philip.nakashima@eng.monash.edu.au

The deformation electron density, $\Delta\rho$, is defined as

$$\Delta\rho = \rho_{total} - \rho_{IAM} \quad (1)$$

where ρ_{total} is the total electron density and ρ_{IAM} is the density associated with a superposition of free, unbonded atoms, otherwise known as the independent atom model (IAM) (*17*, *19*). Given that the total electron density in a crystal can be expressed as a Fourier sum,

$$\rho(\mathbf{r}) = \sum_{\mathbf{g}} F_{\mathbf{g}} \exp(-2\pi i \mathbf{g}.\mathbf{r}) \quad (2)$$

where $F_{\mathbf{g}}$ are the Fourier coefficients of the electron density (structure factors), $\mathbf{g}$ are reciprocal lattice vectors, and $\mathbf{r}$ is a real space vector within the unit cell, Eq. 1 becomes

$$\Delta\rho(\mathbf{r}) = \sum_{\mathbf{g}} (F_{\mathbf{g}} - F_{\mathbf{g}}^{IAM}) \exp(-2\pi i \mathbf{g}.\mathbf{r}) \quad (3)$$

Experimentalists and theorists alike set out to determine the structure factors, $F_{\mathbf{g}}$, as accurately as possible because the differences from IAM structure factors, $F_{\mathbf{g}}^{IAM}$, are typically very small. In aluminum, the main problem has been to determine the three lowest-order structure factors, F_{111}, F_{002}, and F_{022}, with sufficient accuracy, as these contain all of the bonding information and are the only ones to deviate significantly from IAM calculated values (*15*, *16*).

When considering all published sets of $F_{\mathbf{g}}$ including orders up to at least F_{022} (*14*–*17*), it became apparent that the strongest variations in $\Delta\rho$ occur at the centers of the tetrahedral and octahedral interstices. Thus, an appropriate way to summarize the literature is to plot each source as a point on a graph of $\Delta\rho_{oct}$ at the center of the octahedral interstices versus $\Delta\rho_{tet}$ at the center of the tetrahedral interstices. This is done in Fig. 1 (see fig. S1 for individual references). All determinations of $\Delta\rho$ throughout the present work were executed on the basis of ΔF_{111}, ΔF_{002}, and ΔF_{022}, where $\Delta F_{\mathbf{g}} = F_{\mathbf{g}} - F_{\mathbf{g}}^{IAM}$, because both previous work (*15*, *16*) and our own work (*17*) suggest that $\Delta F_{\mathbf{g}} \equiv 0$ for F_{113} and higher orders. All structure factors were converted to $T = 0$ K (*17*) and all charge densities presented here are for $T = 0$ K.

The points corresponding to our QCBED and DFT determinations are circled in Fig. 1. Recent ab initio studies by Ogata *et al*. (*7*) and Kioussis *et al*. (*8*) provide no structure factors. However, the former explicitly describes the high excess total electron density (i.e., positive $\Delta\rho$) in the octahedral hole (also apparent from their 3D plot), whereas the latter explicitly states that excess (i.e., bonding) charge density is preferentially located in the tetrahedral hole. We therefore partition the graph in Fig. 1 to reflect $\Delta\rho_{oct} > \Delta\rho_{tet}$ for (*7*) and $\Delta\rho_{tet} > \Delta\rho_{oct}$ for (*8*). Although the spread of points in the graph is large, most determinations show $\Delta\rho_{tet} > \Delta\rho_{oct}$. Our experimental (QCBED) and theoretical (DFT) results suggest that bonding electron density is almost exclusively located in the tetrahedral hole.

Experiments relying on x-ray diffraction and the kinematic (single scattering) approximation to interpret the data are fundamentally limited by problems of extinction and scale (*20*). These can introduce large systematic errors into the determination of the lowest-order bonding-sensitive structure factors (*14*, *16*, *20*) and contribute to the large spread of experimental points in Fig. 1 (*14*–*17*) (fig. S1). Previous electron diffraction measurements using the critical voltage method (*15*–*17*) are absolute and therefore free of the problems of extinction and scale; however, the method conventionally depends on the validity of the three-beam approximation (*21*, *22*) and it can only access a very limited number of structure factors (F_{111} and F_{002} in aluminum to date), insufficient for a unique and self-consistent determination of $\Delta\rho$.

In QCBED, electrons are focused into very small volumes, allowing regions of perfect crystal

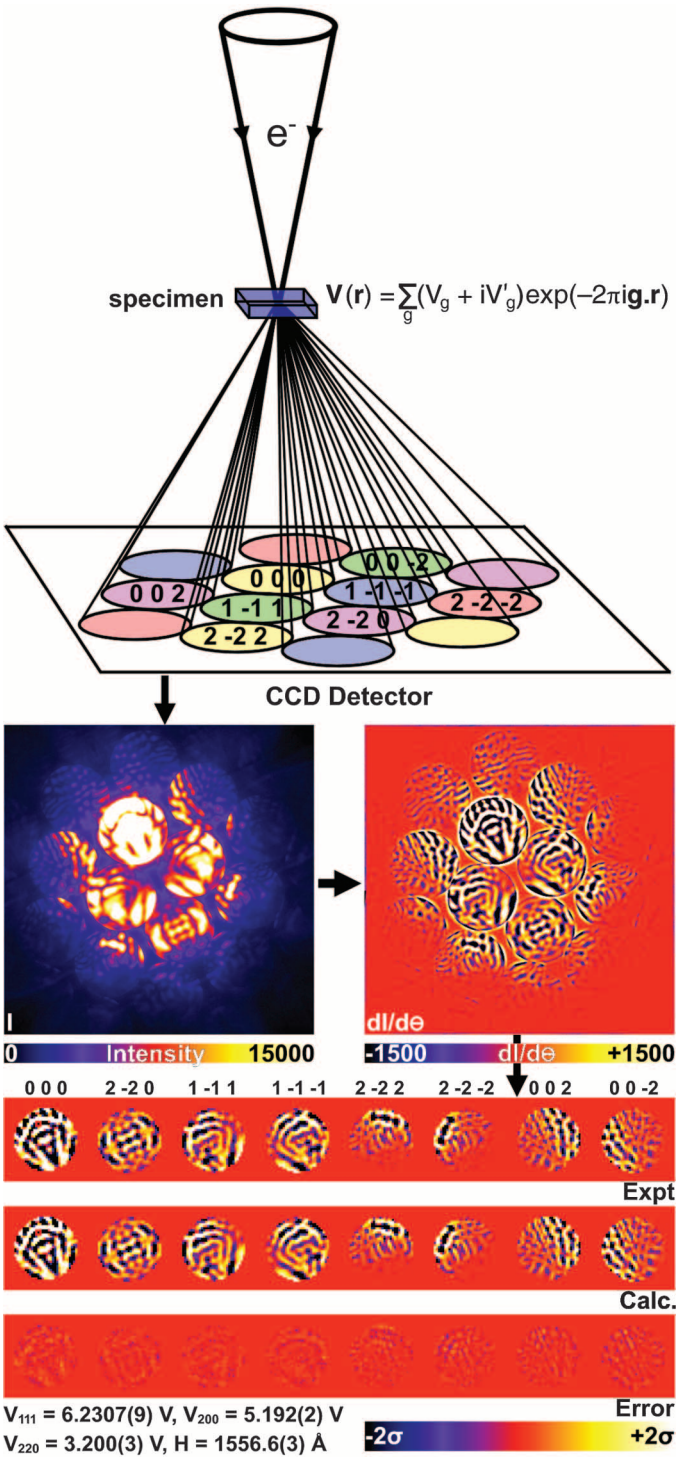

Fig. 2. An incident cone of electrons is scattered by the crystal potential to form a CBED pattern. The as-captured intensities, *I*, can be differentiated with respect to scattering angle according to the approach of (*24*) and then matched with a calculated differential CBED pattern. The parameters refined in fitting are the structure factors, $V_{\mathbf{g}}$, and phenomenological absorption coefficients, $V_{\mathbf{g}}'$, of the most strongly scattering crystal planes; crystal thickness, *H*; and the coordinates of the pattern in reciprocal space. The results for $V_{\mathbf{g}}$ and *H* are reported for this example near [110] and 200.8 keV electrons. The crystal is oriented to satisfy the 2 –2 0 Bragg condition so as to increase the sensitivity to V_{022}. The error map is in units of standard uncertainty per pixel in the experimental data.

to be probed selectively (*17*). The incidence of the electrons over a range of angles (Fig. 2) produces a set of diffracted discs containing intensity oscillations that are highly sensitive to the structure factors of the diffracting crystal planes, the crystal thickness, and the proximity of the relevant reciprocal lattice points to the Ewald sphere. CBED patterns are calculated using a full dynamic (multiple) electron scattering theory (*17*, *23*), making extinction and scale issues irrelevant. Quantitative matching of calculated CBED patterns to experimental ones proceeds by refining the parameters to which they are most sensitive (i.e., the structure factors of the most strongly scattering crystal planes and the crystal thickness) (*17*).

Figure 2 summarizes our QCBED experiments. We apply the angular difference method (*24*) to the as-captured intensities, I, to remove most of the deleterious contributions of inelastic scattering from the resulting difference pattern, $dI/d\theta$, including thermal diffuse scattering (TDS), which cannot be removed by energy-filtering electron optics. CBED patterns were usually acquired with the crystal oriented to satisfy the Bragg condition of a reflection, thereby increasing sensitivity to the corresponding structure factor.

Pattern matching was carried out with the RefineCB program of Zuo (*17*, *23*, *25*), which we modified for 2D near-zone-axis differential QCBED. The variable parameters were the crystal potential structure factors, V_g, of the most strongly scattering crystal planes (i.e., V_{220}, V_{111}, and V_{002} in Fig. 2), their associated absorption potentials, V_g', the crystal thickness, H, and the coordinates defining the position of the CBED pattern in reciprocal space. This amounts typically to about 20 parameters, which are outnumbered by the ~10^4 data points being pattern-matched, resulting in a highly constrained solution. Structure factors measured by QCBED in terms of crystal potential, V_g, were converted to electron density structure factors, F_g, according to the Mott formula (*17*).

In Fig. 2, the output calculated pattern has been matched to the experimental pattern well enough that no difference is detectable without the aid of the error map. This is the difference between the input experimental pattern and the refined calculated pattern expressed in units of uncertainty in each pixel of the experimental pattern. Although some systematic difference remains, its magnitude is small enough to ensure that almost all of the information has been extracted.

The levels of uncertainty in the refined parameters listed at the bottom of Fig. 2, which derive from a single pattern, only reflect the uncertainty in the global minimum of the optimization criterion, χ^2 (*17*), in parameter space. The true precision can only be assessed by repeating structure factor measurements from many CBED patterns collected across a range of experimental conditions.

We have collected 156 CBED patterns from different zone axes, scattering geometries, and crystal thicknesses (~150 to ~2000 Å), with different electron energies and at different temperatures, from 99.9999+% pure aluminum foils electropolished to electron transparency. The QCBED processing of all of these data resulted in the measurement of 14 independent structure factors, each one measured a large number of times, from a total of more than 1 million data points, effectively removing the possibility of a non-unique solution (*17*). The four lowest-order QCBED measured structure factors (converted to F_g and $T = 0$ K) are compared to previously published results and the present DFT calculation in Table 1 [see table S1 and (*17*) for all 14 measured structure factors]. The uncertainty of the

Table 1. A comparison of the four lowest-order structure factors of aluminum determined in the present work (QCBED) at ambient and low temperatures, as well as by Wien2K [DFT with GGA/FPLAPW +lo +ls (*18*)], the literature (mean of all x-ray diffraction measurements, mean of all ab initio calculations, mean of all critical voltage measurements), and the IAM (*19*). F_{111} and F_{113} were not measured at low temperature, and critical voltage measurements have never extended beyond F_{002}. The Debye-Waller factors, $B_{ambient} = 0.81641$ Å^2 (*17*, *31*) and $B_{low\ temp.} = 0.52945$ Å^2 (*17*), were used for the QCBED measurements at ambient and low temperatures, respectively (*17*). Uncertainties are given in parentheses as one standard deviation of the mean and apply to the last significant digit.

F_g (e$^-$/atom)	QCBED (ambient) (this work)	QCBED (low temp.) (this work)	Mean of x-ray expts. (*14*–*17*)	Mean of ab initio (*15*–*17*)	Wien2K DFT (this work)	Mean of critical voltage (*15*–*17*)	IAM (*19*)
1 1 1	8.87(1)		8.8(2)	8.86(7)	8.87	8.87(2)	8.95
0 0 2	8.37(2)	8.37(1)	8.4(2)	8.40(9)	8.38	8.38(2)	8.50
0 2 2	7.32(8)	7.31(3)	7.3(1)	7.31(7)	7.30		7.31
1 1 3	6.64(6)		6.61(9)	6.65(5)	6.64		6.65

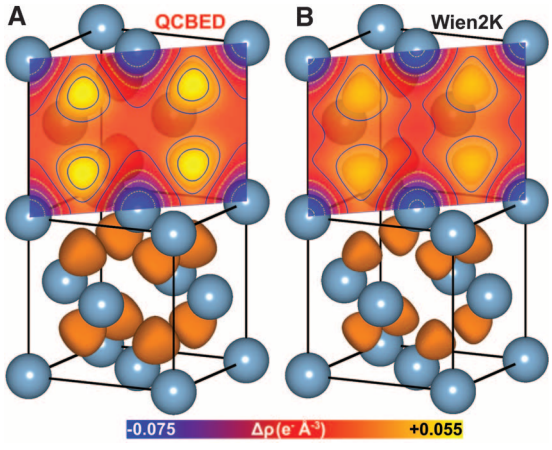

Fig. 3. (**A** and **B**) The $\Delta\rho = 0.0275$ e$^-$ Å^{-3} isosurface (corresponding to 50% of $\Delta\rho_{max}$ for the QCBED determination) is drawn in the lower unit cell for the present QCBED and DFT (Wien2K) determinations, respectively. The top cell is {110} plane-sectioned to show the contour plots of $\Delta\rho$ in these planes, which pass through both the tetrahedral and octahedral interstices as defined in the inset of Fig. 1. Contours are at 0.02 e$^-$ Å^{-3} intervals, with the first dark contour showing $\Delta\rho = 0$ e$^-$ Å^{-3}. Dark solid contours show $\Delta\rho > 0$ and light dashed lines $\Delta\rho < 0$. The color scale indicates the value of $\Delta\rho$ for all surfaces and sections. All $\Delta\rho$ values were computed using Eden Crystallography (*29*). Plots were generated using VESTA (*30*).

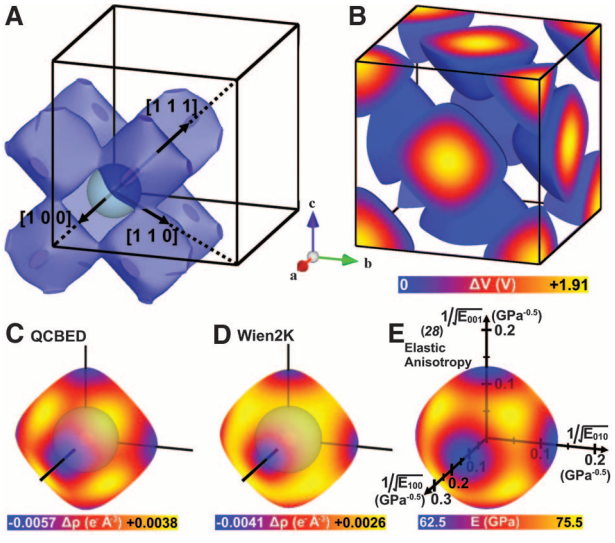

Fig. 4. (**A**) The 20% $\Delta\rho_{max}$ (QCBED) isosurface is plotted about a single atom together with principal lattice vectors originating from the atomic site. (**B**) The $\Delta V = 0$ (QCBED) isosurface is plotted and the volume enclosed is colored according to the deformation potential due to chemical bonding, ΔV. The atoms are localized at the maxima of ΔV. (**C** and **D**) Plots of $\Delta V = 0$ as a surface and colored according to $\Delta\rho$ intersected by the surface for our QCBED and DFT work, respectively. (**E**) The surface represents $1/\sqrt{E_{uvw}}$ (where E_{uvw} is Young's modulus in direction [*uvw*]), calculated from the anisotropic elastic constants of aluminum (*28*). The surface coloring represents the magnitude of E_{uvw}. All $\Delta\rho$ and ΔV values were computed using Eden Crystallography (*29*). Plots were generated using VESTA (*30*).

QCBED measurements of F_{111} and F_{002} at 300 K is an order of magnitude lower than published x-ray diffraction measurements and about 5 times as precise as the mean values of published ab initio determinations (Table 1 and table S1).

The high uncertainty in F_{022} measured by QCBED at ambient temperatures and x-ray diffraction is probably due to aluminum's low-frequency, transverse acoustic phonon mode with wave vectors in the {0*hh*} planes associated with the rigid body movement of atomic chains along ⟨011⟩ (*26*, *27*). To test this hypothesis, we collected 16 CBED patterns near ⟨001⟩ with the use of a liquid helium specimen stage. The diffuse background and its structure in these patterns were significantly reduced relative to equivalent ambient temperature patterns (*17*), giving visual evidence of reduced scattering from phonons. The low-temperature QCBED measurements of F_{022} are much more precise than at ambient temperatures, with the uncertainty now comparable to the uncertainties in the lower-order structure factors measured by QCBED (Table 1 and table S1). This suggests that the spread in F_{022} measured at ambient temperatures is phonon-mediated.

The increased precision of F_{022} shows that there is almost no bonding information in this structure factor and that deviations from F_g^{IAM} only occur for F_{111} and F_{002}. This implies that critical voltage measurements to date (Table 1 and table S1) are sufficient to determine the bonding electron density distribution in aluminum; however, this conclusion could not have been reached earlier because of the large variation in previous F_{022} measurements (*14*–*16*).

Using F_{111}, F_{002}, and F_{022} from QCBED at ambient temperatures and our Wien2K (*18*) DFT calculation (GGA/FPLAPW +lo +ls), we obtained the maps of bonding electron density (*17*) shown in Fig. 3. The $\Delta\rho = 0.0275$ $e^- Å^{-3}$ isosurfaces (corresponding to $0.5\Delta\rho_{max}$ determined by QCBED) show that electron accumulation occurs in the tetrahedral interstices in both cases. The {110} plane-sectioned contour plots show that there is near-zero bonding density in the octahedral holes according to the QCBED measurements, whereas there is slight antibonding density associated with the octahedral hole in the DFT determination. A stronger accumulation in the tetrahedral holes is indicated by QCBED than by the Wien2K DFT calculation. Although there are some quantitative differences in Δρ between the QCBED and DFT determinations, the form of the bonding electron distribution is almost the same. Of all previous determinations represented by points in Fig. 1 (and fig. S1), our DFT-calculated Δρ is the closest to the present QCBED benchmark Δρ measurement.

An important problem in materials science is the effect of interatomic bonding on the mechanical properties of materials (*2*–*4*, *7*–*9*, *11*, *12*). The seminal work of Eberhart (*4*) has demonstrated a strong correlation between the topology of the total electron density, ρ_{total}, and the anisotropy of elastic constants in metals (*4*, *28*). In that study (*4*) and related work (*8*), ρ_{total} was determined from ab initio theoretical calculations. Given that ρ_{total} is dominated by ρ_{IAM} (Eq. 1), which contains no bonding information, a complementary alternative to the topological analysis of Eberhart (*4*) might be to consider Δρ only. The reliability of such an approach depends heavily on the accuracy with which ρ_{total} (and thus Δρ) can be determined.

Figure 4A presents the $0.2\Delta\rho_{max}$ isosurface surrounding each atom in aluminum as determined by QCBED. This level was chosen to show how the bonding density differs in the three principal directions drawn (i.e., [100], [110], and [111]). The [100] vector does not intersect the drawn isosurface, whereas [110] intersects it at the necking point between edge-sharing tetrahedra and [111] passes directly through the main pocket of bonding density and the center of the tetrahedral hole. Thus, among these three directions, bonding is strongest along [111] and weakest along [100]. If Young's modulus, E_{uvw}, is proportional to Δρ in any particular direction [*uvw*], then Fig. 4A suggests that $E_{100} < E_{110} < E_{111}$, which is indeed the case (*28*).

A more sophisticated method for relating chemical bonding to elastic anisotropy might be developed by considering both Δρ and the deformation potential due to bonding, Δ*V*, where, analogously to Eq. 1,

$$\Delta V = V_{total} - V_{IAM} \quad (4)$$

where V_{total} is the total crystal potential and V_{IAM} is that of a superposition of free (unbonded) atoms. In Fig. 4B, the $\Delta V = 0$ (QCBED) isosurface is plotted and bounds the positions of the atoms. Figure 4C examines this isosurface plotted around a single atom, and the surface is colored according to Δρ that it passes through. The same is done for the present DFT calculation in Fig. 4D. The plots for the present QCBED and DFT determinations bear a strong resemblance to one another.

A heuristically determined physical relationship between the $\Delta V = 0$ isosurface, Δρ, and Young's modulus, E_{uvw}, is detailed in (*17*). It suggests that E_{uvw} is proportional to Δρ in any particular direction and proportional to $1/r^2_{\Delta V=0}$ (where $r_{\Delta V=0}$ is the distance from the atomic site to the $\Delta V = 0$ isosurface). To represent this, $1/\sqrt{E_{uvw}}$ is plotted as a surface in Fig. 4E. This surface is colored by the magnitude of E_{uvw} determined from the anisotropic elastic constants in (*28*). Figure 4E is a close match, in terms of form and relative magnitude, to the QCBED- and DFT-generated plots in Fig. 4, C and D, respectively. A more quantitative analysis of the correlation between Young's modulus and chemical bonding, as determined by our QCBED measurements and DFT calculation, in the principal directions shown in Fig. 4A is given in fig. S3 and (*17*).

Our work shows both experimentally and theoretically that interatomic bonding is tetrahedrally centered in aluminum, with almost no bonding electron density in the octahedral interstice. Bonding is shown to have a direct correlation with mechanical properties—that is, the anisotropic elastic constants—in the present case of aluminum.

References and Notes

1. M. Clugston, R. Flemming, *Advanced Chemistry* (Oxford Univ. Press, Oxford, 2008), p. 83.
2. A. Cottrell, *Introduction to the Modern Theory of Metals* (Institute of Metals, London, 1988).
3. E. H. Medlin, R. E. Dingle, D. W. Field, *Nature* **224**, 581 (1969).
4. M. E. Eberhart, *Acta Mater.* **44**, 2495 (1996).
5. J. Sprösser-Prou, A. vom Felde, J. Fink, *Phys. Rev. B* **40**, 5799 (1989).
6. *World Metal Statistics Yearbook* (World Bureau of Metal Statistics, Hertfordshire, UK, 2006), pp.12–68.
7. S. Ogata, J. Li, S. Yip, *Science* **298**, 807 (2002).
8. N. Kioussis, M. Herbranson, E. Collins, M. E. Eberhart, *Phys. Rev. Lett.* **88**, 125501 (2002).
9. R. S. Leigh, *Philos. Mag.* **42**, 139 (1951).
10. J. Hafner, *Z. Phys. B* **22**, 351 (1975).
11. C. Woodward, D. R. Trinkle, L. G. Hector Jr., D. L. Olmsted, *Phys. Rev. Lett.* **100**, 045507 (2008).
12. J. M. MacLaren, S. Crampin, D. D. Vvedensky, M. E. Eberhart, *Phys. Rev. Lett.* **63**, 2586 (1989).
13. M. Morinaga, S. Nasu, H. Adachi, J. Saito, N. Yukawa, *J. Phys. Condens. Matter* **3**, 6817 (1991).
14. N. N. Sirota, *Acta Crystallogr. A* **25**, 223 (1969).
15. W. Hoppe, R. Mason, Eds., *Advances in Structure Research by Diffraction Methods* (Pergamon, Oxford, 1975), pp. 221–225.
16. A. G. Fox, M. A. Tabbernor, R. M. Fisher, *J. Phys. Chem. Solids* **51**, 1323 (1990).
17. See supporting material on *Science* Online.
18. P. Blaha, K. Schwarz, P. Sorantin, S. B. Trickey, *Comput. Phys. Commun.* **59**, 399 (1990).
19. P. A. Doyle, P. S. Turner, *Acta Crystallogr. A* **24**, 390 (1968).
20. P. Coppens, *X-ray Charge Densities and Chemical Bonding* (Oxford Univ. Press, New York, 1997).
21. A. F. Moodie, J. R. Sellar, D. Imeson, C. J. Humphreys, *J. Electron Microsc.* **26** (suppl.), 191 (1977).
22. A. F. Moodie, C. J. Humphreys, D. Imeson, J. R. Sellar, in *Electron Diffraction 1927–1977*, P. J. Dobson, J. B. Pendry, C. J. Humphreys, Eds. (Institute of Physics, Bristol, UK, 1978), chap. 3.
23. J. M. Zuo, *Rep. Prog. Phys.* **67**, 2053 (2004).
24. P. N. H. Nakashima, B. C. Muddle, *Phys. Rev. B* **81**, 115135 (2010).
25. J. M. Zuo, M. Kim, M. O'Keeffe, J. C. H. Spence, *Nature* **401**, 49 (1999).
26. N. B. Brockhouse, A. T. Stewart, *Phys. Rev.* **100**, 756 (1955).
27. G. Honjo, S. Kodera, N. Kitamura, *J. Phys. Soc. Jpn.* **19**, 351 (1964).
28. J. F. Nye, *Physical Properties of Crystals* (Oxford Univ. Press, Oxford, 1985).
29. J. R. Somoza, A. Szöke, H. Szöke, *Acta Crystallogr. A* **57**, 678 (2001).
30. K. Momma, F. Izumi, *J. Appl. Crystallogr.* **41**, 653 (2008).
31. D. L. McDonald, *Acta Crystallogr.* **23**, 185 (1967).

32. We thank M. Weyland for assisting in the collection of the liquid helium–temperature CBED data; A. F. Moodie and A. W. S. Johnson for their expert readership and valuable suggestions; J. M. Zuo for sharing his RefineCB code, which we have modified to execute our QCBED analysis; J. Shih for electropolishing some of the specimens; the Victorian Partnership for Advanced Computing (VPAC); and the Australian Research Council (ARC) for infrastructure grant LEO454166. P.A. thanks V. A. Streltsov, A. W. S. Johnson, and the late E. N. Maslen for their guidance.

Supporting Online Material

www.sciencemag.org/cgi/content/full/331/6024/1583/DC1
Materials and Methods
Figs. S1 to S3
Table S1
References

1 October 2010; accepted 1 February 2011
10.1126/science.1198543